Single-crystal and powder electron-nuclear double resonance of $RbCl:O_2^-$: A comparison between the spin Hamiltonian parameters obtained from both experiments

S. Van Doorslaer, F. Callens, F. Maes, and E. Boesman
Laboratory for Crystallography and Study of the Solid State, Krijgslaan 281-S1, B-9000 Gent, Belgium
(Received 8 November 1994; revised manuscript received 30 January 1995)

In this work a single-crystal ENDOR study of $RbCl:O_2^-$ is presented. The angular variation of two sets of ^{85}Rb and ^{87}Rb ENDOR transitions is investigated. The corresponding superhyperfine (SHF) and nuclear-quadrupole coupling tensors are determined. These ENDOR results can be explained only by assuming a monovacancy model, i.e., O_2^- replacing a single Cl^- ion. The linewidth of the EPR signals is shown to be determined by the Rb SHF interaction. The corresponding powder ENDOR study of $RbCl:O_2^-$ is also presented. The powder ENDOR spectra could be simulated using the single-crystal data. Finally, from this simulation procedure a fitting program is derived to obtain information from powder ENDOR spectra of analogous systems.

I. INTRODUCTION

In the past, it has been frequently shown that electron-nuclear double resonance (ENDOR) studies of impurity centers in single-crystal samples lead to the determination of the total defect structure. Often, however, no single crystals are available. In such cases, powder ENDOR may form an alternative method to obtain information about the total structure of the defect. In this work, we make a comparison between the information obtainable for both powder and single-crystal ENDOR studies of the O_2^- defect in RbCl.

X_2^- defects (X=O,S,Se) in alkali halide single crystals have been studied extensively with electron paramagnetic resonance (EPR).[1–12] For some of these defects, the EPR studies did not determine unambiguously the total defect structure. The monovacancy model was sometimes questioned and a divacancy model, in which the X_2^- molecule is replacing two halide ions, was also considered.

From the work of Känzig and co-workers,[1–3] Vannotti and Morton,[4,5] and Callens and co-workers,[6–12] it is known that, depending on the lattice, the paramagnetic p lobes of the X_2^- defect may be oriented along a $[\bar{1}10]$ or a [001] direction. To explain the occurrence of a specific type in an alkali halide single crystal, three effects should be considered: Coulombic, covalency, and steric effects. A full determination of the total defect structure is therefore necessary.

ENDOR investigations on a whole series of X_2^- defects (X=O,S,Se) in different alkali halide crystals were started.[13] Zeller and Känzig[2] detected a well-resolved superhyperfine (SHF) interaction in the EPR spectra of the O_2^- defect in KCl. From these data, a monovacancy model was proposed for the $KCl:O_2^-$ case. Although no resolved SHF structure was found in the $RbCl:O_2^-$ EPR spectrum, Zeller and Känzig[2] also assumed a monovacancy model for this center.

In this article, the validity of this model is investigated using single-crystal and powder ENDOR.

II. EXPERIMENTAL TECHNIQUES

The single crystals were grown by the Bridgman method. RbCl powder (Merck) was mixed with 1% KO_2 (Merck). The crystals thus obtained were x-ray irradiated at room temperature (RT) for typically $\frac{1}{2}$ h with a tungsten anticathode Philips x-ray tube, operated at 60 kV and 40 mA. Powder ENDOR was performed on ground crystals. The powders were x-ray irradiated at RT during 1 h.

The EPR spectra were recorded using a Bruker ESP 300 X-band spectrometer, with maximum microwave power 200 mW. The detection conditions were 8 K and 1 mW microwave power.

The ENDOR spectra were recorded on the same spectrometer, equipped with a Bruker ESP 353E ENDOR/Triple extension (EN 374 rf amplifier with a maximum power of 200 W and an EN 525 Schomandl synthesizer). The best detection conditions were 8 K and 200 mW microwave power at maximum rf power. The rf was modulated at 12.5 kHz with a modulation depth of 100 kHz.

III. RESULTS AND DISCUSSION

A. EPR spectra

1. Single-crystal EPR spectra

Zeller and Känzig[2] investigated the O_2^- defect in RbCl with EPR. The orthorhombic center has been found to have the following g tensor: $g_x=1.9836$, $g_y=1.9846$, and $g_z=2.2947$ with corresponding axes parallel to $[\bar{1}10]$, [001], and [110]. As shown by Shuey and Zeller,[3] the paramagnetic p lobe corresponds to the x direction (smallest g value) and the largest g value is found along the molecular axis (z direction). The linewidth of the EPR signals was ascribed to an unresolved superhyperfine structure.

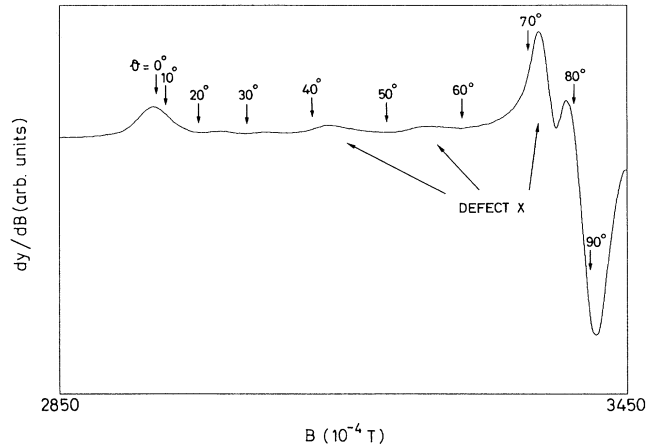

FIG. 1. Powder spectrum of the O_2^- defect in RbCl (taken at 8 K, with 1 mW microwave power).

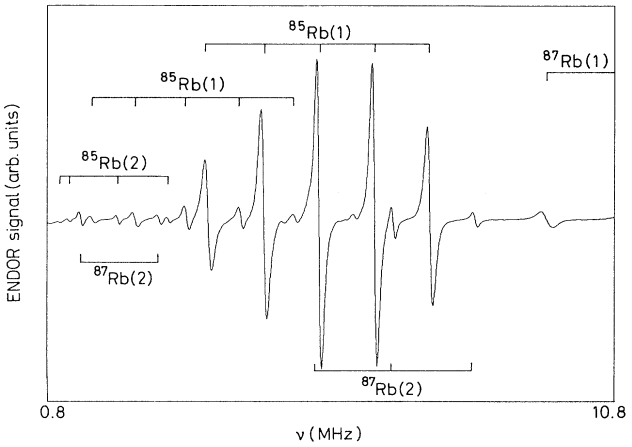

FIG. 3. Experimental single-crystal ENDOR spectrum of RbCl:O_2^- ($\mathbf{B}_0\|[110]$, $T=8$ K). The ENDOR transitions due to ^{85}Rb interaction 1 and interaction 2 (both isotopes) are marked.

2. *Powder EPR spectra*

The EPR powder spectrum is given in Fig. 1. The fact that $g_x \approx g_y$ is reflected in the EPR spectrum (signal typical for a system with an axial g tensor). In the spectrum another EPR signal of an orthorhombic defect is seen (defect X in Fig. 1). The defect X was found regardless of whether the crystal was first irradiated and then ground or vice versa. Since no indication of this defect was found in the single-crystal EPR spectra, a surface defect is proposed. This signal is found not to influence the ENDOR results.

B. Single-crystal ENDOR spectra

1. *General remarks*

In the ENDOR spectra transitions belonging to ^{85}Rb and ^{87}Rb are found. The interactions are labeled 1 and 2, because of the accordance with the Rb interactions observed in the ENDOR spectra of RbCl:S_2^-.[13]

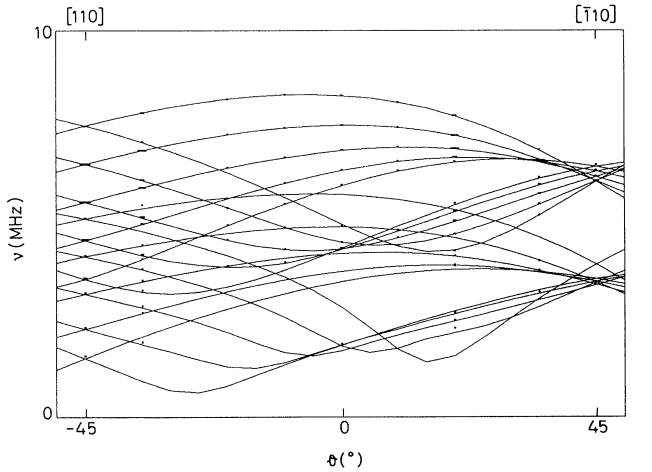

FIG. 2. ^{85}Rb angular variation in plane 1 for interaction 1. Rectangles: experimental points; lines: theoretical angular variation calculated using the values of Table I.

2. *ENDOR spectra corresponding to Rb interaction 1*

The ENDOR angular variations for the Rb SHF interaction (both isotopes) are measured in the g_x-g_z plane ($\mathbf{B}_0\perp[001]$) and in the plane containing the g_y axis ($\mathbf{B}_0\perp[100]$ or $\mathbf{B}_0\perp[010]$). The first plane is called plane 1, the latter is labeled 2. One of the angular variations for both isotopes is shown in Fig. 2. In Fig. 3 a typical ENDOR spectrum is shown.

To analyze the spectra, the standard Hamiltonian for a single nucleus ($I > \frac{1}{2}$) coupled with an unpaired electron ($S=\frac{1}{2}$) is used:

$$\hat{\mathbf{H}}=\beta\hat{\mathbf{S}}^T\overleftrightarrow{g}\mathbf{B}+\hat{\mathbf{I}}^T\overleftrightarrow{A}\hat{\mathbf{S}}-\beta_N\hat{\mathbf{I}}^T\overleftrightarrow{g}_N\mathbf{B}+\hat{\mathbf{I}}^T\overleftrightarrow{Q}\hat{\mathbf{I}}\ . \tag{1}$$

The analysis of the ENDOR frequencies was done by complete diagonalization of the spin Hamiltonian matrix. In Table I, the principal values and corresponding axes of the hyperfine (A) and nuclear quadrupole (Q) tensors are given. In Fig. 2, the full lines correspond to the theoretical angular variations, calculated using Table I.

TABLE I. Principal values (in MHz) and axes of the ^{85}Rb and ^{87}Rb superhyperfine and nuclear-quadrupole tensors for interaction 1.

			Angles with respect to		
	^{85}Rb	^{87}Rb	g_x	g_y	g_z
A_x	11.49	38.95	39.8	90	129.8
A_y	6.52	22.08	90	0	90
A_z	6.30	21.36	−50.2	90	39.8
Q_x	0.33	0.52	78.7	90	168.7
Q_y	−0.23	−0.36	90	0	90
Q_z	−0.10	−0.16	−11.3	90	78.7

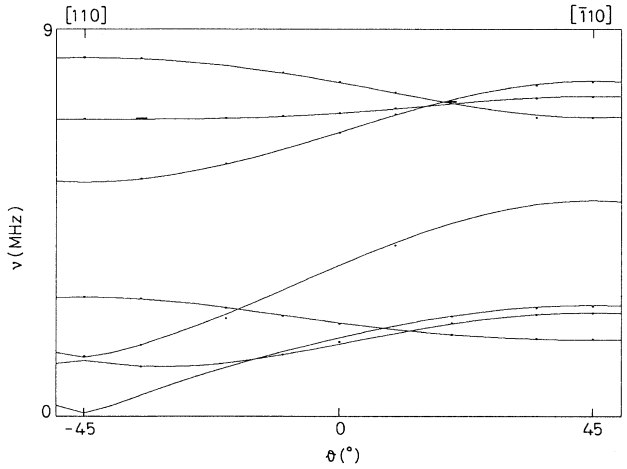

FIG. 4. ^{87}Rb angular variation in plane 1 for interaction 2. Rectangles: experimental points; lines: theoretical angular variation calculated using the values of Table II.

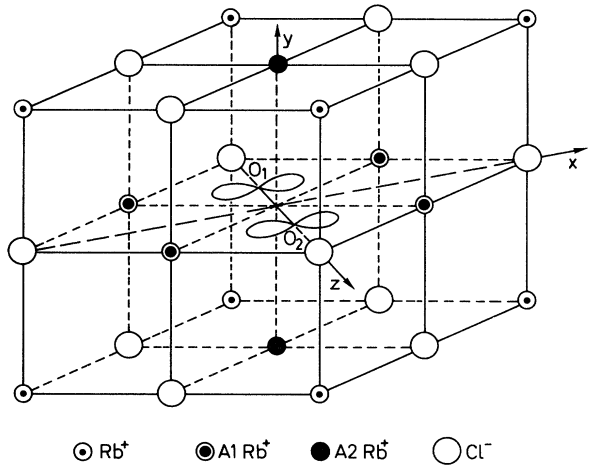

FIG. 5. Monovacancy model of O_2^- in RbCl. The Rb^+ ions labeled A1 are responsible for interaction 1, those labeled A2 are causing interaction 2.

3. *ENDOR spectra corresponding to Rb interaction 2*

The ENDOR angular variations are measured in planes 1 and 2. Figure 4 shows one of these angular variations.

The spectra were analyzed in the same way as before. Table II shows the principal values and corresponding axes of the A and Q tensors. The theoretical angular variations calculated using Table II are shown in Fig. 4 (full lines).

Although ENDOR experiments give no direct information about the sign of the A principal values, they are taken all negative. This choice of signs will be discussed later.

4. *Discussion*

As mentioned in the Introduction, Zeller and Känzig[2] assumed that the O_2^- molecule was filling up a monovacancy, replacing a single Cl^- ion (Fig. 5). In what follows, this assumption will be confirmed and additional evidence and information will be given. The observed Rb interaction 1 will be shown to be due to the nearest-neighboring Rb nuclei in the g_x-g_z plane (Fig. 5, A1). Interaction 2 is caused by the nearest Rb nuclei along the [001] axis (Fig. 5, A2).

In what follows, the discussion will be held for the ^{85}Rb interactions, unless mentioned otherwise. Analogous derivations can be made for the ^{87}Rb interaction.

a. Superhyperfine interactions. Zeller and Känzig[2] proved that, since the g value corresponding to the [1̄10] axis (g_x) is the smallest value, the unpaired electron resides most of the time in a molecular orbital of the form $(p_{x1}-p_{x2})/\sqrt{2}$ (the $|\Gamma_2^+\rangle$ state), where 1 and 2 denote the different oxygen atoms. Due to spin-orbit coupling, admixture of $|\Gamma_4^+\rangle$ and $|\Gamma_1^+\rangle$ should be considered. The resulting ground state of the center can then be described as follows:[2]

$$|\psi\pm\rangle=\cos\alpha|\Gamma_2^+\rangle|\pm\tfrac{1}{2}\rangle\pm i\sin\alpha|\Gamma_4^+\rangle|\pm\tfrac{1}{2}\rangle \pm\frac{\lambda}{2E}(\cos\alpha-\sin\alpha)|\Gamma_1^+\rangle|\mp\tfrac{1}{2}\rangle\ , \quad (2)$$

with $\tan(2\alpha)=\lambda/\Delta$, $|\pm\frac{1}{2}\rangle$ the eigenstates of $\hat{\mathbf{S}}_z$, and in which Γ_1^+, Γ_4^+, and Γ_2^+ are irreducible representations of the D_{2h} symmetry group.[14] In Eq. (2), Δ and E are crystal-field parameters and λ denotes the positive spin-orbit coupling constant. Zeller and Känzig[2] found that, for the RbCl:O_2^- case, $\lambda/\Delta=0.1379$, $\lambda/E=0.0006$, $\cos\alpha=0.9977$, and $\sin\alpha=0.068\,46$.

To explain the SHF components both covalency effects and point dipolar contributions have to be taken into account.

Neglecting point dipolar contributions, Shuey and Zeller[3] derived expressions for the SHF components of the four Rb nuclei A1 *(interaction 1)*. The wave function for the unpaired electron in the neighborhood of alkali-metal nucleus 1 is assumed to be as follows:

TABLE II. Principal values (in MHz) and axes of the ^{85}Rb and ^{87}Rb superhyperfine and nuclear-quadrupole tensors for interaction 2.

			Angles with respect to		
	^{85}Rb	^{87}Rb	g_x	g_y	g_z
A_x	−1.53	−5.17	0	90	90
A_y	−1.16	−3.93	90	0	90
A_z	−1.63	−5.54	90	90	0
Q_x	0.09	0.14	0	90	90
Q_y	0.21	0.34	90	0	90
Q_z	−0.30	−0.48	90	90	0

$$|\psi\pm\rangle \approx \cos\alpha(c_\sigma\phi_\sigma + c_s\phi_s)|\pm\tfrac{1}{2}\rangle \pm i\sin\alpha c_\pi\phi_\pi|\pm\tfrac{1}{2}\rangle \ , \quad (3)$$

where

$$\phi_\sigma = -(4p)_x\cos\delta + (4p)_z\sin\delta \ ,$$
$$\phi_\pi = (4p)_y \ , \quad (4)$$
$$\phi_s = (4s) \ ,$$

and δ is the angle between the g_x axis and the ϕ_σ lobe. As a first approximation, this lobe is oriented along the axis connecting the Rb nucleus and the nearest oxygen nucleus. The O-O distance and the Rb-Cl distance along a $\langle 100\rangle$ axis are taken as 0.128 nm (Ref. 15) and 0.328 nm, respectively, which leads to a value for δ of 36.0°.

Using wave function (3), the components of the SHF matrix are given by

$$A^c_{yy} = A_s - \tfrac{2}{3}A_\sigma - A_\pi\cos\delta \ ,$$
$$A^c_{xx} = A_s + A_\sigma(\tfrac{1}{3} + \cos2\delta) + A_\pi\cos\delta \ ,$$
$$A^c_{zz} = A_s + A_\sigma(\tfrac{1}{3} - \cos2\delta) - \tfrac{10}{3}A_\pi\cos\delta \ , \quad (5)$$
$$A^c_{zx} = -A_\sigma\sin2\delta - A_\pi\sin\delta \ ,$$
$$A^c_{xz} = -A_\sigma\sin2\delta - \tfrac{10}{3}A_\pi\sin\delta \ ,$$

wherein the superscript c denotes covalency and A_s, A_σ, and A_π (in MHz) are defined in the following way:

$$A_s = \cos^2\alpha c_s^2\frac{8\pi}{3}|\psi(0)|^2_{\text{alk}}\left[\frac{\mu_0}{4\pi h}g_N g_e\beta\beta_N 10^{-6}\right] \ ,$$
$$A_\sigma = \cos^2\alpha c_\sigma^2\tfrac{3}{5}\left\langle\frac{1}{r^3}\right\rangle_{\text{alk}}\left[\frac{\mu_0}{4\pi h}g_N g_e\beta\beta_N 10^{-6}\right] \ , \quad (6)$$
$$A_\pi = \sin2\alpha c_\sigma c_\pi\frac{3}{5}\left\langle\frac{1}{r^3}\right\rangle_{\text{alk}}\left[\frac{\mu_0}{4\pi h}g_N g_e\beta\beta_N 10^{-6}\right] .$$

On the other hand, the SHF components due to the point dipolar contribution in a system with anisotropic g tensor are given as follows:[16]

$$A^d_{ij} = \frac{\mu_0}{4\pi}\frac{\alpha_N}{r^3}g_j(3r_i r_j - \delta_{ij}) \quad (i,j = x,y,z) \ ,$$

with

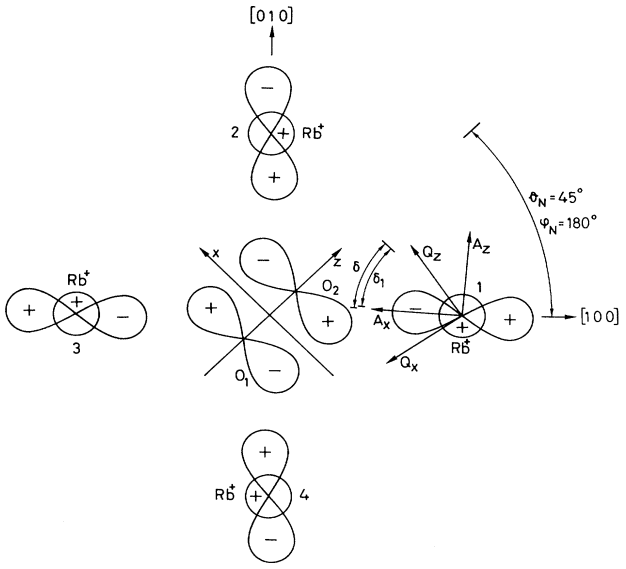

FIG. 6. Direction of the principal axes of the Rb SHF and nuclear-quadrupole tensors. δ is the angle between the ϕ_σ lobe and the g_x axis; δ_1 is the angle between the A_x axis and the g_x axis.

$$\alpha_N = \beta\beta_N\frac{g_N}{h}$$

and

$$r_x = \cos\phi_N\sin\theta_N \ ,$$
$$r_y = \sin\phi_N\sin\theta_N \ , \quad (7)$$
$$r_z = \cos\theta_N \ ,$$

the direction cosines of the nucleus with respect to the g tensor axes. θ_N and ϕ_N equal 45° and 180°, respectively (see Fig. 6). r is the distance between the defect (assumed to be a point) and the nucleus at which the contribution is calculated.

By adding the corresponding components A^d_{ij} and A^c_{ij}, a nonsymmetrical A matrix is obtained. The symmetrical tensor $[A]^T[A]$ can easily be diagonalized and compared with the experimental data in the following way:

$$\begin{bmatrix}\cos\delta_1 & 0 & -\sin\delta_1\\ 0 & 1 & 0\\ \sin\delta_1 & 0 & \cos\delta_1\end{bmatrix}\begin{bmatrix}A_{xx} & 0 & A_{zx}\\ 0 & A_{yy} & 0\\ A_{xz} & 0 & A_{zz}\end{bmatrix}\begin{bmatrix}A_{xx} & 0 & A_{xz}\\ 0 & A_{yy} & 0\\ A_{zx} & 0 & A_{zz}\end{bmatrix}\begin{bmatrix}\cos\delta_1 & 0 & \sin\delta_1\\ 0 & 1 & 0\\ -\sin\delta_1 & 0 & \cos\delta_1\end{bmatrix}$$
$$= \begin{bmatrix}(11.49\ \text{MHz})^2 & 0 & 0\\ 0 & (6.52\ \text{MHz})^2 & 0\\ 0 & 0 & (6.30\ \text{MHz})^2\end{bmatrix} , \quad (8)$$

wherein δ_1 corresponds to the experimentally found tilt angle between the A_x axis and the g_x axis (39.8°) (see Fig. 6). From Eq. (8) we are able to calculate values for r, A_s, A_π, and A_σ. With $\delta = 36.0°$, it was not possible to fit the hyperfine values exactly. However, when taking the δ value equal to 40.8°, an exact fit was possible. This change of δ can be expected, since ϕ_σ was only taken along the Rb-O direction in a first approach. Figure 6

shows that the value of δ is physically acceptable. The values thus obtained for the coefficients c_s^2, c_π^2, and c_σ^2 are given in Table III. The distance r between the center of the O_2^- molecule and the Rb nucleus is found to be 0.328 nm, which is the expected value for a RbCl lattice.

Table III shows that the values of the coefficients in the RbCl:O_2^- case are about three times smaller than for the RbCl:S_2^- case. This was expected, since the S_2^- molecule is larger than the O_2^- molecule. The effect of the larger molecule is reflected especially in the c_s^2 and c_σ^2 coefficients, because for both molecules the overlap between the X_2^- Γ_2^+ orbitals (X=O,S) and the Rb σ orbitals is larger than the overlap between the X_2^- Γ_4^+ orbitals and the Rb π orbitals. In this way, the change in the X_2^- molecule will mainly be noticed in the c_σ^2 and c_s^2 coefficients, rather than in the c_π^2 coefficients.

For the magnetic point dipolar tensor, the diagonal elements are A_x^d=0.47 MHz, A_y^d=−0.22 MHz, and A_z^d=−0.23 MHz. The axis corresponding to the largest value is tilted 39.5° away from the g_x axis. The deviation of this tilt angle from 45° is due to the inclusion of the anisotropic g tensor into Eq. (7).

As mentioned in the Introduction, Zeller and Känzig[2] ascribed the linewidth of the EPR signals to an unresolved SHF interaction with the Rb A1 nuclei. Up to first order, the SHF splitting K for the $\mathbf{B}_0$ field parallel to one of the g-tensor axes can be related to the SHF matrix elements A_{ij} (in MHz) in the following way:[18]

$$\mathbf{B}_0\|g_x \text{ axis: } K\ (10^{-4}\text{ T})=\frac{\sqrt{A_{xx}^2+A_{zx}^2}}{\beta g_x},$$

$$\mathbf{B}_0\|g_y \text{ axis: } K\ (10^{-4}\text{ T})=\frac{A_{yy}}{\beta g_y}, \tag{9}$$

$$\mathbf{B}_0\|g_z \text{ axis: } K\ (10^{-4}\text{ T})=\frac{\sqrt{A_{zz}^2+A_{xz}^2}}{\beta g_z}.$$

The specific values for the ^{85}Rb and ^{87}Rb splittings are mentioned in Table IV.

To simulate the resulting EPR line, the presence of both isotopes with natural abundance and the fact that four equivalent Rb ions contribute to the observed interaction have to taken into account. The linewidths of the EPR signals thus obtained are given in Table V. Comparison with the experiment[2] proves that the observed linewidths of the EPR lines are indeed due to a SHF interaction with the four nearest-neighboring Rb nuclei.

TABLE IV. ^{85}Rb SHF splittings (in 10^{-4} T) for some specific directions of the magnetic field, calculated using the ENDOR results.

	$\mathbf{B}_0\|$	^{85}Rb	^{87}Rb
K	[$\bar{1}$10]	3.49	11.83
K	[001]	2.35	7.96
K	[110]	2.74	9.29

For *interaction 2,* the principal axes of both A and Q tensors are parallel to the g-tensor axes. The only reasonable possibility that does not lower the orthorhombic-I symmetry of the A and Q tensors is that of the two nearest-neighboring Rb^+ ions along the [001] axis (Fig. 5, A2).

From symmetry considerations, it is found that no atomic valence orbital of these Rb^+ ions can interact with the O_2^- Γ_2^+ orbitals and only the $4p_z$ orbital mixes with O_2^- Γ_4^+ orbitals (see Fig. 7).

As mentioned in Sec. III B 3, the sign of the principal A values is taken negative. For this choice of signs, the following considerations are taken into account. Since no direct coupling occurs, the isotropic contribution must be due to spin polarization and/or configuration interaction. This isotropic part can be either positive or negative.

Now, considering a negative isotropic part (A_{iso}=−1.44 MHz in an approximation where orbital contribution is neglected), the resulting anisotropic part is (−0.09 MHz, 0.28 MHz, −0.19 MHz). Using Eq. (7) with θ_N and ϕ_N equal to 90° and 0°, respectively, and R=0.328 nm, the following values are obtained for the point dipole contribution: −0.21, 0.43, and −0.25 MHz. These are clearly too large in absolute values. However, Eq. (7) does not account for the distribution in space of the paramagnetic electron over the O_2^- ion. Taking this distribution[19] into account leads to the following results: A_x^d=−0.11 MHz, A_y^d=0.31 MHz, and A_z^d=−0.21 MHz. This is almost exactly the observed anisotropic part. This justifies the choice of signs for the A components.

b. The nuclear-quadrupole tensor. For both interactions, the nuclear-quadrupole tensor has the same symmetry as the SHF tensor A, as expected. For interaction 1, the axes of the Q tensor are not parallel to those of the A tensor, although this was approximately the case for

TABLE III. Comparison between the calculated coefficients c_s^2, c_π^2, and c_σ^2 obtained from the ENDOR results for RbCl:O_2^- (a) and RbCl:S_2^- (b), taking into account that $|\psi(0)|_{4s}^2=29.28\times10^{25}$ cm^{-3} and $\langle r^{-3}\rangle_{4p}=20.24\times10^{25}$ cm^{-3} (Ref. 17).

	c_s^2	c_σ^2	c_π^2	$c_\pi c_\sigma$
(a)	0.000 651	0.003 30	0.000 587	0.001 39
(b)	0.002 14	0.009 79	0.000 59	0.002 41

TABLE V. Comparison between the EPR linewidths (in 10^{-4} T) obtained from the ENDOR results (a) and those obtained experimentally by Zeller and Känzig (Ref. 2) (b).

$\mathbf{B}_0\|$	ΔB (a)	ΔB (b)
[$\bar{1}$10]	32.1	31.8
[001]	22.0	21.3
[110]	25.1	26.0

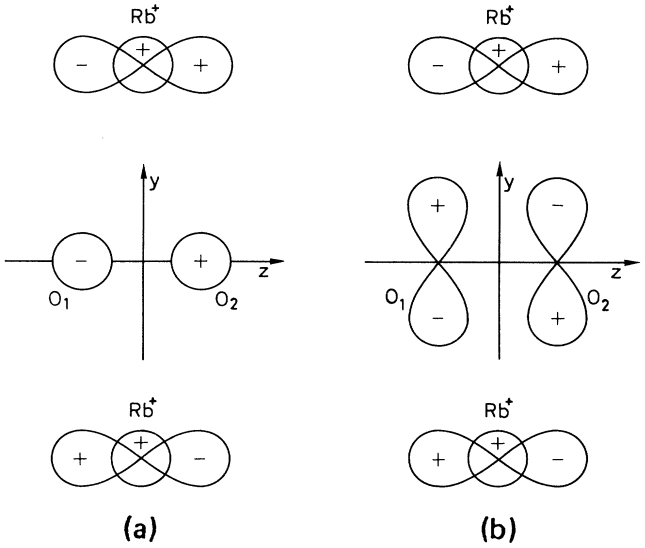

FIG. 7. Rb^+ ions responsible for interaction 2. (a) No interaction between Rb highest valence orbitals and the $O_2^-\Gamma_2^+$ orbitals. (b) Interaction between the Rb p_z orbitals and the $O_2^-\Gamma_4^+$ orbitals.

the S_2^- defect in RbCl.

To calculate the nuclear-quadrupole tensor, the field gradient has to be determined. The elements of the field gradient tensor[20] are given by

$$V_{\alpha\beta}=\frac{e}{4\pi\varepsilon_0}\frac{\partial^2(1/r)}{\partial\alpha\partial\beta}\quad(\alpha,\beta=x,y,z)\ . \tag{10}$$

In a point approximation (i.e., the defect is approximated by an electron centered on a lattice position), the principal axes of the field gradient tensor are oriented along the [100], [010], and [001] axes. If $I\geq 1$, the nucleus has an axially symmetrical charge distribution. Hence, at the nearest-neighboring cation sites, the Q tensor will be axial, with its symmetry axis in the radial direction of the defect (i.e., along a ⟨100⟩ axis). For an electron in an

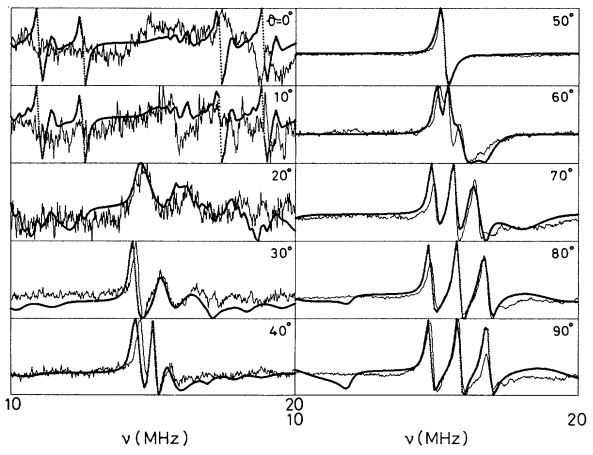

FIG. 8. Comparison between the experimental (full lines) and theoretical (++++) "angular variation" of the powder ENDOR spectra in the 10–20 MHz region.

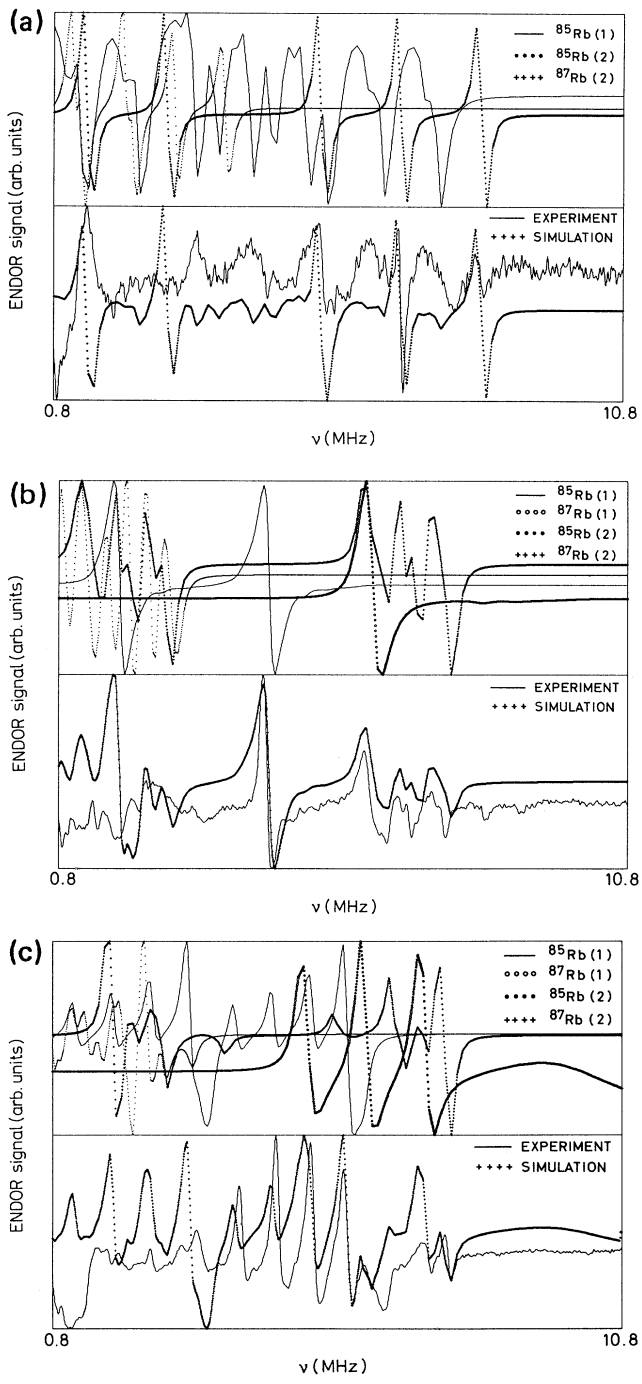

FIG. 9. For the angles $\theta=0°$ (a), 50° (b), and 90° (c) are given (1) the simulated powder ENDOR spectra for each of the interactions (both isotopes); (2) Comparison between the experimental ENDOR spectrum and the simulation resulting from addition of the spectra shown in (1).

atom or molecule, however, Eq. (14) must be integrated over the wave function. For atomic orbitals the calculation parallels that of magnetic dipolar coupling. For many-electron systems, a summation over all electrons should be considered. This can break the axial symmetry of the Q tensor.

Figure 5 shows that both oxygen atoms are at equal distance from the Rb A2 nuclei but one of the oxygen atoms is closer to Rb nucleus A1 than the other. This explains why the Q tensor of interaction 2 has an orthorhombic-I symmetry, where the Q tensor of interaction 1 is tilted in the (001) plane. This tilt is not necessarily the same as that of the A tensor, since it depends on the specific values of the tensor components.

c. Remarks. The above analysis is based on the assumption of the validity of the monovacancy model for the O_2^- center in RbCl. However, the possibility of finding a correspondence between the ENDOR characteristics and the surrounding Rb nuclei of the defect proves the validity of the model. All trials to fit other models (e.g., the divacancy model) to our ENDOR results have failed.

C. Powder ENDOR spectra

1. The ENDOR spectra

To determine the positions in the EPR powder spectra to measure the ENDOR spectra, the g tensor is taken to be axial. For an axial case, the following expression for g^2 is known:

$$g^2=g_\perp^2\sin^2\theta+g_\parallel^2\cos^2\theta \tag{11}$$

where θ denotes the angle between $\mathbf{B}_0$ and the $g_\parallel$ axis.

For our specific case, $g_\parallel=g_z$ and $g_\perp$ is taken to be the average of g_x and g_y (1.9841). The value of θ was varied from 0° to 90° in steps of 10°. For the corresponding resonance fields, the ENDOR spectra were measured (see Fig. 1). In this way, a sort of "angular variation" is obtained. Some of the experimental spectra are shown in Figs. 8 and 9.

2. Discussion

Our first goal was to simulate the powder ENDOR spectra using the SHF and nuclear-quadrupole parameters obtained from the single-crystal ENDOR study. Once this objective can be successfully realized, a fitting program can be constructed to get useful information from other powder ENDOR studies.

Equation (1) is the starting point for a discussion on the effects of quadrupole interactions on ESR and ENDOR spectra. Since the electronic Zeeman energy is by far the largest, the direction of quantization z' for the electron spin can be taken to be along $l_{z'}$ (Ref. 20)

$$l_{z'}=\frac{l\cdot\vec{\vec{g}}}{g} \tag{12}$$

where

$$g^2=l\cdot\vec{\vec{g}}\cdot\vec{\vec{g}}\cdot l\ .$$

The electron Zeeman energy is diagonalized if we refer the electron spin to a set of axes whose z component lies along this direction. This is obtained by replacing $\hat{S}$ by $l_{z'}\hat{S}_{z'}$. Equation (1) then becomes

$$\hat{H}=g\beta B_0\hat{S}_{z'}+\hat{\mathbf{I}}^T\cdot\vec{\vec{A}}\cdot l_{z'}\hat{S}_{z'}-g_N\beta_N B_0\hat{\mathbf{I}}^T\cdot l+\hat{\mathbf{I}}^T\cdot\vec{\vec{Q}}\cdot\hat{\mathbf{I}}$$

with

$$\mathbf{B}=B_0 l\ . \tag{13}$$

Combination of Eqs. (12) and (13) gives us

$$\begin{aligned}\hat{H}|M_S\rangle=&g\beta B_0 M_S|M_S\rangle\\&+\hat{\mathbf{I}}^T\cdot\left[\frac{M_S}{g}l\cdot\vec{\vec{g}}\cdot\vec{\vec{A}}-g_N\beta_N B_0 l\right]|M_S\rangle\\&+\hat{\mathbf{I}}^T\cdot\vec{\vec{Q}}\cdot\hat{\mathbf{I}}|M_S\rangle\ .\end{aligned} \tag{14}$$

Using (14) we find for the energy of state $|M_S,M_I\rangle$

$$\begin{aligned}E(M_S,M_I)=&g\beta B_0 M_S+G(M_S)M_I\\&+\tfrac{3}{2}q(M_S)[M_I^2-\tfrac{1}{3}I(I+1)]\end{aligned} \tag{15}$$

with

$$[G(M_S)]^2=l\cdot\left[\frac{M_S}{g}\vec{\vec{g}}\cdot\vec{\vec{A}}-g_N\beta_N B_0\vec{\vec{U}}\right]\cdot\left[\frac{M_S}{g}\vec{\vec{A}}\cdot\vec{\vec{g}}-\beta_N g_N B_0\vec{\vec{U}}\right]\cdot l\ ,$$

$$[G(M_S)]^2q(M_S)=l\cdot\left[\frac{M_S}{g}\vec{\vec{g}}\cdot\vec{\vec{A}}-g_N\beta_N B_0\vec{\vec{U}}\right]\cdot\vec{\vec{Q}}\cdot\left[\frac{M_S}{g}\vec{\vec{A}}\cdot\vec{\vec{g}}-g_N\beta_N B_0\vec{\vec{U}}\right]\cdot l\ .$$

$\vec{\vec{U}}$ is the unit matrix. Since the SHF interaction term is larger than the nuclear Zeeman term, the latter term can be neglected. This leads to

$$\begin{aligned}[G(M_S)]^2&=\frac{M_S^2}{g^2}[l\cdot\vec{\vec{g}}\cdot\vec{\vec{A}}\cdot\vec{\vec{A}}\cdot\vec{\vec{g}}\cdot l]\ ,\\[G(M_S)]^2q(M_S)&=\frac{M_S^2}{g^2}[l\cdot\vec{\vec{g}}\cdot\vec{\vec{A}}\cdot\vec{\vec{Q}}\cdot\vec{\vec{A}}\cdot\vec{\vec{g}}\cdot l]\ .\end{aligned} \tag{16}$$

$q(M_S)$ is now independent of M_S. For the energy of the ESR transitions ($\Delta M_S=1,\Delta M_I=0$), there is up to first order no contribution from the quadrupole interaction [see Eq. (15)]. The magnetic resonance field B_r is then given by

$$B_r=\frac{h\nu_{\mathrm{EPR}}-M_I[l\cdot\vec{\vec{g}}\cdot\vec{\vec{A}}\cdot\vec{\vec{A}}\cdot\vec{\vec{g}}\cdot l]^{1/2}}{g} \tag{17}$$

with

$$h\nu_{\mathrm{EPR}}=\Delta E_{\mathrm{EPR}} \quad (\Delta M_S=1\ ,\ \ \Delta M_I=0)\ .$$

The EPR spectrum of a ground material (powders) reflects an average of all molecular orientations with respect to the external magnetic field. Every value of the magnetic field in the EPR spectrum corresponds with a set of molecular orientations. When simulating powder ENDOR spectra, we have to determine which orientations are selected when saturating the EPR signal. From Eq. (17) the set of direction vectors l corresponding to a particular value of B_r can be determined. In this way, a selection can be made in the molecular orientations that contribute to an ENDOR powder spectrum. This is called the "orientation selection" principle, introduced by Rist and Hyde.[21–23]

Once the molecular orientations are known, the ENDOR transitions (also depending on l), can be calculated. Indeed, Eq. (16) leads to ($\Delta M_S=0, \Delta M_I=1$)

$$\nu_{\mathrm{NMR}}=\frac{1}{h}[G(M_S)+\tfrac{3}{2}q(M_S)(2M_I\pm 1)] \tag{18}$$

with

$$|M_I|\neq I\ .$$

In practice, the simulation occurs as follows.[24,25] The input consists of the g, A, and Q tensor, the EPR linewidth Γ_{EPR} (in 10^{-4} T), the ENDOR linewidth Γ_{ENDOR} (in kHz), the g_N value, and the resonance field B_{res} at which the ENDOR spectra are measured. Using Eq. (17) the B_r values are calculated for each l direction in space. [Note that for an $I=\frac{3}{2}$ ($\frac{5}{2}$) system four (six) B_r values correspond with one l direction.] These values are stored in the matrices BMAT1 to BMAT4 (BMAT6). With Γ_{EPR} as full width at half maximum, a Gaussian is constructed with top B_{res}. To every element of the matrices BMAT1 to BMAT4 (BMAT6) a weight factor is assigned corresponding to this Gaussian. All orientations l_s for which this weight factor is larger than 0.05 are held back. For the selected molecular orientation l_s, the nuclear resonances [Eq. (18)] are calculated. A Lorentzian line shape with linewidth Γ_{ENDOR} is centered on these nuclear resonances. The final ENDOR powder spectrum is obtained by adding all spectra corresponding with the selected molecular orientations, taking into account the appropriate weight factor.

In Fig. 8, the full "angular variation" of both the experimental spectra and the simulations is given in the 10–20 MHz region. In this region, the highest-frequency line of ^{87}Rb interaction 1 is seen. For θ ranging from 20° to 90°, the simulations are very good, especially since the ENDOR line intensities were not taken into account. For the two other angles, there is a difference between experiment and simulation. This difference is not due to an error in the simulation procedure, but to an experimental problem. Since $\theta=0°$ corresponds with the selection of the g_z direction, the powder and single-crystal ENDOR spectra should resemble each other. This is the case for the simulation, but not for the experimental powder ENDOR spectrum. Probably the detection conditions were not sufficient for that angle.

In Figs. 9(a)–9(c), the experimental powder ENDOR spectra are compared with the simulations in the 0.8–10.8 MHz region, for $\theta=0°$, 50°, and 90°. In this low-frequency region, four interactions have to be considered: interactions 1 and 2 for both isotopes ^{85}Rb and ^{87}Rb. In these spectra, the effect of not considering the line intensities is clearly visible. Nevertheless, the simulations are still very good. For $\theta=0°$, we notice that ^{87}Rb interaction 2 is clearly visible. The ENDOR transitions corresponding with ^{85}Rb interaction 1 are also detected, but their intensity is a lot smaller than for the other angles. The experimental detection conditions have apparently changed in favor of interaction 2.

After finding that most information from the single-crystal ENDOR spectra is also present in the ENDOR powder spectra, the next step is to withdraw this information from these spectra. There are two ways to construct a fitting program. Either the total powder ENDOR spectra are simulated using some arbitrary starting parameters and compared with the experimental spectra or the positions of the ENDOR peaks in the simulated powder ENDOR spectra are used to compare with the experiment. Because our simulation procedure does not take into account the ENDOR line intensities of each peak, the second approach was used.

A lot of problems arose when trying to fit the powder ENDOR results. When the starting values are taken very different from the exact values, the fitting procedure gets trapped in local minima. The local minima values will not lead to a good simulation of the ENDOR spectra for all angles. The only solution to this problem is an iterative restart of the program with different starting values.

Secondly, due to the fact that the line intensities are not taken into account, slight shifts of the line positions can occur in the theoretical spectra with respect to the experimental results. Clear examples are shown in Fig. 8. The experimental and theoretical line positions sometimes differ due to the line shape. This has an effect on the accuracy of the calculations. Finally, due to the large amount of calculations done in each step of the iteration, the program is rather slow.

These three problems imply that it is better to analyze the ENDOR spectra visually before starting to fit. The shape of the powder "angular variation" reveals a lot of details about the considered SHF interaction. Equation (11) shows that the ENDOR spectrum corresponding with $\theta=0°$ contains information about the [110] (g_z) orientation, whereas the spectrum corresponding to $\theta=90°$ includes information about the [$\bar{1}$10](g_x) and [001](g_y) directions. In Fig. 10, the "angular variations" of two cases are considered:

(a) A and Q tensors have an orthorhombic-I symmetry;

(b) the A and Q tensors are tilted in the (001) plane, with the tilting angles different for both tensors.

For both cases the g tensor is taken orthorhombic and the interacting nucleus has a nuclear spin $\frac{3}{2}$.

For the first case, all the lines of the angular variation reach an extreme at $\theta=0°$ and 90°. In the $\theta=0°$ spectra, two groups of three equidistant signals are found. The positions of the signals at $\theta=0°$ contain information about

the absolute values of the A and Q components in the [110] direction (A_z and Q_z). In the ENDOR spectra corresponding with $\theta=90°$ four groups of equidistant signals are found. This leads to two A and two Q components. It is not immediately clear which set of components corresponds to which direction. Simulation of the spectra for all angles solves this problem. Another interesting feature is the crossing of the lines in the angular plot. This indicates that the sign of Q_y and Q_x will be different from that of Q_z. This could also be derived from the fact that $|Q_x|+|Q_y|=|Q_z|$.

In the second case [Fig. 10(b)], there are only in the $\theta=90°$ spectra two groups of three equidistant lines. This means that either the [001] or [$\bar{1}$10] direction is a principal axis for the A and Q tensors. The corresponding SHF parameters can easily be found. Notice again the crossing of the three lines, indicating that the sign of the obtained Q component will be opposite to that of Q_z.

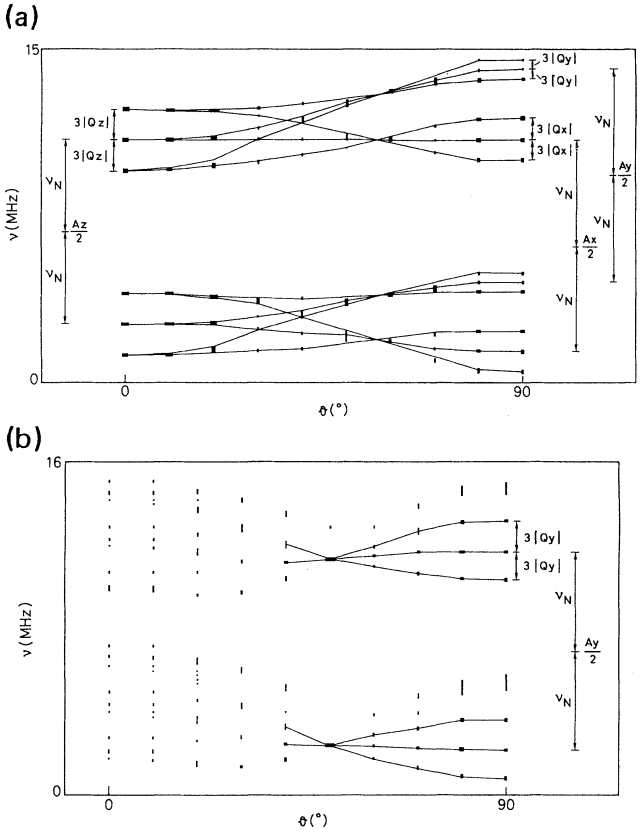

FIG. 10. The powder "angular" variation of two cases. (a) A and Q tensors have an orthorhombic-I symmetry. $A_x([\bar{1}10])=12.17$ MHz, $A_y([001])=18.8$ MHz, $A_z([110])=13.5$ MHz, $Q_x([\bar{1}10])=-0.34$ MHz, $Q_y([001])=-0.14$ MHz, $Q_z([110])=0.48$ MHz. (b) The A and Q tensors are tilted in the (001) plane over different angles. $A_x([\bar{1}10]+\alpha)=24.46$ MHz, $A_y([001])=13.8$ MHz, $A_z([110]+\alpha)=13.54$ MHz, $\alpha=35°$, $Q_x([\bar{1}10]+\beta)=0.75$ MHz, $Q_y([001])=-0.49$ MHz, $Q_z([110]+\beta)=-0.26$ MHz, $\beta=80°$. The g tensor is taken orthorhombic, and the interaction nucleus has a nuclear spin $\frac{3}{2}$.

It should be mentioned that sometimes the "angular plot" of case (b) can resemble the one of case (a) (for instance when the deviation of orthorhombic-I symmetry is small). In such a case, however, the Q components derived from the spectra for $\theta=0°$ and 90°, will never form a traceless Q tensor, indicating that at least two axes of the Q tensor must differ from the g-tensor axes.

To interpret our specific ENDOR spectra, the highest-frequency lines of interaction 1 are considered first. The angular variation is given in Fig. 11. This is an ideal starting point, since the lines are isolated from the other interactions. Based on the knowledge of the g_N values of the Rb isotopes, there is no doubt that a ^{87}Rb nucleus is responsible for the interaction. Since the $\theta=90°$ spectrum shows three quidistant ENDOR signals (Fig. 8) and since the considered lines clearly reach extremes at this angle (Fig. 11), one of the A and Q principal axes is probably parallel to either the [001] or [$\bar{1}$10] axis. The corresponding A component is about 22.2 MHz and the Q component has an absolute value of 0.35 MHz. Its sign will be opposite to that of the Q component along an axis closest to the [110] direction.

To fit the powder spectra, both possibilities for the principal axis were considered. Only when [001] was taken as a principal axis could the fitting be done in a satisfying way. The results are presented in Table VI.

Table VI shows that the obtained SHF and nuclear-quadrupole parameters differ somewhat from the single-crystal parameters (the error is about 2.5%). These errors can be ascribed to the shift of the line positions as mentioned before.

The analysis of interaction 2 is difficult, due to the overlap with the ENDOR signals of ^{85}Rb interaction 1 in the 0–10 MHz region. Indications of the second interaction are found in the ENDOR spectra for $\theta=0°$–20°, where interaction 1 is less detectable. The fact that for $\theta=0°$ three equidistant ENDOR signals are found means that the [110] direction is a principal axis of the A and Q tensors. $A_z=5.5$ MHz and $|Q_z|$ is 0.47 MHz. In the $\theta=90°$ spectrum the overlap with the signals of interaction 1 is too large to conclude anything about the values

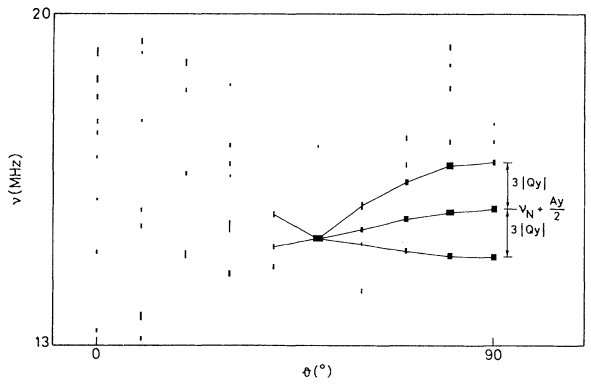

FIG. 11. Experimental powder ENDOR "angular variation" for interaction 1 (highest-frequency lines).

TABLE VI. Principal values (in MHz) and axes for the ^{87}Rb SHF and nuclear-quadrupole tensor of interaction 1, obtained from powder ENDOR analysis.

	^{87}Rb	Difference with single-crystal results (Table I)
Tilt angle	38°	1.8°
A_x	37.87	1.07
A_y	22.16	0.08
A_z	21.74	0.38
Tilt angle	80°	1.3°
Q_x	0.60	0.08
Q_y	−0.34	0.02
Q_z	−0.26	0.10

of the A and Q components. One ENDOR signal [the line at highest frequency in Fig. 9(c)] is isolated from the group of lines due to interaction 1. The angular variation of this line reaches an extreme at $\theta=90°$, which might indicate that the [001] and consequently the [$\bar{1}$10] directions are principal axes of the A and Q tensors. This conclusion, however, is not absolute, since there is no proof that two groups of three quidistant ENDOR lines are present.

Analysis of the powder ENDOR spectra thus leads to the conclusion that two Rb interactions are visible. For interaction 1, the A and Q tensors are tilted in the (001) plane. The corresponding principal values are given in Table VI. The second interaction is found to have one axis parallel to the molecular axis of O_2^-. The corresponding A and Q components are smaller than those of interaction 1.

For interaction 1, the same discussion can be made as in the single-crystal case. Although the A and Q principal values are not as accurate as in the single-crystal case, the conclusion is the same: the O_2^- defect is located in a monovacancy. For interaction 2, the only conclusion that can be made is that the interaction with the Rb A2 nuclei is one of the possible causes, since one of the A and Q tensor axes is parallel to the molecular axis.

Until now, one important feature has been omitted in our discussion. From the powder EPR spectrum, the orientation of the g-tensor axes cannot be determined unambiguously. Consequently, ENDOR measurements will only lead to determination of the A- and Q-tensor axes relative to the g-tensor axes. However, from the knowledge of the host lattice, the number of possibilities can be limited. Indeed, assuming a monoclinic or triclinic g-tensor symmetry would lead to more than two inequivalent interactions with neighboring Rb^+ ions, which are not observed. Since g_x is almost equal to g_y, an axial symmetry around a [111] axis may be considered too. In this case however, the principal axes of the Rb SHF interactions are all expected to be different from the g-tensor axes. When taking an orthorhombic symmetry, the g-tensor axes can either be along the crystal axes or along the [$\bar{1}$10], [001], and [110] axes.

In the first case (the g-tensor axes parallel to the crystal axes), symmetry considerations for the nearest-neighboring Rb^+ ions in a monovacancy model lead to the following conclusions:

(a) the SHF and nuclear-quadrupole tensor axes should be along the g-tensor axes;

(b) three sets of inequivalent interactions with the nearest-neighboring Rb^+ ions should be found.

Since only two inequivalent interactions are found and since the SHF tensor axes do not parallel the g-tensor axes, this hypothesis has to be rejected. Therefore the g-tensor axes are along the [$\bar{1}$10], [001], and [110] axes. The divacancy model can be rejected for the same reason as mentioned in the discussion of the single-crystal ENDOR spectra.

Although less accurate information could be derived from the powder ENDOR analysis, the results are still sufficient to explain the defect structure. Combination of this technique and knowledge of the lattice structure may be a valuable alternative to investigate defect structures when no single crystals are available.

IV. CONCLUSION

The single-crystal ENDOR spectra of RbCl:O_2^- allowed a detailed analysis of two sets of ^{85}Rb and ^{87}Rb interactions. The orientations of the principal axes of the A and Q tensors of these interactions are in agreement with the overall D_{2h} symmetry of the O_2^- ion in the crystal.

The largest interaction is caused by the nearest-neighboring Rb ions in the (001) plane. Some information about the wave function of the unpaired electron in the neighborhood of these Rb nuclei could be derived. The linewidth of the EPR signals was found to be due to this SHF interaction.

The Rb^+ ions responsible for the second interaction are the two nearest-neighboring cations along the [001] axis. The only model consistent with these ENDOR data is that of an O_2^- molecular ion substituting for a Cl^- ion.

Using the data obtained from the single-crystal ENDOR study, the powder ENDOR spectra could be simulated. From this simulation procedure a fit program was constructed to retrieve information from powder ENDOR spectra, when single crystals are not available.

ACKNOWLEDGMENTS

This work is part of a project sponsored by "Interuniversitair Instituut voor Kernwetenschappen" (IIKW), Belgium. S.V.D. and F.C. would like to thank the NFSR, Belgium, for financial support.

[1]W. Känzig and M. H. Cohen, Phys. Rev. Lett. **3**, 509 (1959).
[2]H. R. Zeller and W. Känzig, Helv. Phys. Acta **40**, 845 (1967).
[3]R. T. Shuey and H. R. Zeller, Helv. Phys. Acta **40**, 873 (1967).
[4]L. E. Vannotti and J. R. Morton, Phys. Rev. **161**, 282 (1967).
[5]L. E. Vannotti and J. R. Morton, Phys. Lett. **24A**, 250 (1967).
[6]P. Matthys, F. Callens, and E. Boesman, Solid State Commun. **45**, 1 (1983).
[7]R. Callens, F. Callens, P. Matthys, and E. Boesman, Phys. Status Solidi B **148**, 683 (1988).
[8]F. Callens, F. Maes, P. Matthys, and E. Boesman, J. Phys. Condens. Matter **1**, 6912 (1989).
[9]F. Maes, F. Callens, P. Matthys, and E. Boesman, J. Phys. Chem. Solids **51**, 1289 (1990).
[10]F. Maes, F. Callens, P. Matthys, and E. Boesman, Phys. Status Solidi B **161**, K1 (1990).
[11]F. Maes, P. Matthys, F. Callens, and E. Boesman, Solid State Commun. **80**, 583 (1991).
[12]F. Maes, P. Matthys, F. Callens, P. Moens, and E. Boesman, J. Phys. Condens. Matter **4**, 249 (1992).
[13]S. Van Doorslaer, F. Maes, F. Callens, P. Moens, and E. Boesman, J. Chem. Soc. Faraday Trans. **90**, 2541 (1994).
[14]G. F. Koster, J. O. Dimack, R. G. Wheeler, and H. Satz, *Properties of the Thirty-Two Point Groups* (MIT Press, Cambridge, MA, 1963).
[15]*Tables of Interatomic Distances and Configurations in Molecules and Ions,* edited by L. E. Sutton (Chemical Society, London, 1958), p. M69.
[16]G. C. Hurst, T. A. Henderson, and R. W. Kreilick, J. Am. Chem. Soc. **107**, 7294 (1985).
[17]A. K. Koh and D. J. Miller, At. Data Nucl. Data Tables **33**, 235 (1985).
[18]M. Iwasaki, J. Magn. Reson. **16**, 417 (1974).
[19]J. A. Pople and D. L. Beveridge, *Approximate Molecular Orbital Theory* (McGraw-Hill, New York, 1970), pp. 27–29.
[20]N. M. Atherton, *Principles of Electron Spin Resonance* (Ellis Horwood, London, 1993).
[21]G. Rist and J. Hyde, J. Chem. Phys. **49**, 2449 (1968).
[22]G. Rist and J. Hyde, J. Chem. Phys. **52**, 4532 (1970).
[23]G. Rist and J. Hyde, J. Chem. Phys. **52**, 4643 (1970).
[24]P. Moens, F. Callens, P. Matthys, and R. Verbeeck, J. Chem. Soc. Faraday Trans. **90**, 2653 (1994).
[25]J. Hütterman, in *EMR of Paramagnetic Molecules,* edited by L. J. Berliner and J. Reuben, Biological Magnetic Resonance Vol. 13 (Plenum, New York, 1993).